Application Case: Airfoil Broadband Noise

Marc C. JACOB
Département d'Aérodynamique Energétique & Propulsion, ISAE-SUPAERO
10 av. Edouard Belin, B.P. 54032, Toulouse Cedex 4
FRANCE

marc.jacob@isae.fr

Special thanks: This document has been prepared with inputs from contributors J. Boudet, E. Jondeau, B. Li J. Caro, N. Grosjean and R. Camussi.

ABSTRACT

This lecture illustrates how the concepts developed along the previous lectures are applied to a popular subject of aeroacoustics: airfoil broadband noise. In particular the motivations for such investigations and the non-standard approaches used to tackle this topic are presented. In order to show a more detailed study than a general paper about airfoil aeroacoustics would allow, the scope is limited to the topic of tip leakage noise. Many of the experimental approaches shown here are also applicable or have been applied to other airfoil noise sources. However, a few ideas described hereafter have been specifically developed for the tip leakage study.

1.0 MOTIVAT ION

Fan broadband noise is one of the dominant sources of modern aircraft in approach flight conditions. This trend is confirmed on UHBR low-geared engines

An inventory of the aerodynamic sources that are present in fan-OGV systems and more generally in ducted rotor-stator configurations can be crudely divided in three types as to the part of the airfoils that are involved: interaction noise, trailing edge self noise and tip leakage noise. Interaction noise is agreed to be the dominant source: steady flow distortions (on blades) or large incoming disturbances result in tonal noise whereas small eddies are sources of broadband noise when they hit the blade or vane leading edges. Trailing edge noise is due to turbulent eddies from the airfoil boundary layers that are swept past the trailing edges resulting in broadband sources and to possible vortex shedding at the trailing edges that are responsible for tonal or quasi tonal noise. These sources have been thoroughly investigated by all means since the early advances of aeroacoustics.

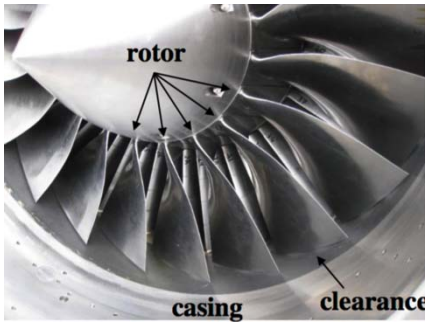

Fig 1-1 Fan tip clearance

Tip leakage noise is the noise induced by the leakage flows that are forced at the blade tips by the rotor motion with respect to the casing walls and/or by the intake boundary layer interacting with the rotor blades (Fig 1-1). Moreover the wakes of the tip flows interact with the tips of the stator vanes: this source can be seen as part of the rotor-stator interaction. In modern turboengines, the tip gaps between the blades and the casing are minimal, but due to the blade elasticity and the blade sweep, the gaps increase when the engine runs at reduced power. It is unclear if the source is significant or not since it is impossible to separate it from other sources on a real rotor-stator stage.

Other sources may be related to tip flows such as rotating instabilities whose onset is suspected to be triggered by blade tip vortices [1] but this mechanism encompasses the whole rotor leading essentially to tonal noise. Finally, buzz-saw noise is also generated at the blade tips but is due the local supersonic flow

conditions, leading to the severe shocks that appear mainly at take off and are also azimuthally linked. This noise source is not due to the tip leakage flow and constitutes a field of research on its own, especially because of the high level tones that propagate non-linearly in the inlet duct [2]. One reason we decided to investigate tip leakage noise, was that as our first investigations on tip leakage noise started, there had been quite many aerodynamic tip leakage flow studies [10]-[17] but very few aeroacoustic ones, most being dedicated to complete fans [18]-[23].

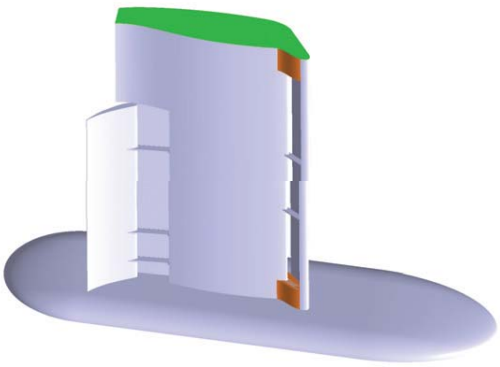

Fig 1-2 Flap side edge at JAXA/RTRI

Another reason was that a quite similar mechanism is at work on flap side edges, with a particular resemblance at the flap/body junction in some high-lift designs. As can be seen on Fig 1-2 showing a mock-up tested at the JAXA-LWT2 and RTRI wind tunnels.

In order to facilitate thorough aerodynamic and acoustic measurements and also to be compatible with airframe noise configurations, a generic fixed non-rotating single blade configuration was defined during PROBAND, an EU project on broadband noise in turboengines.

Several experimental campaigns and numerical simulations have been carried out on the tip leakage flow configuration [3]-[5] that will be described in the next section. Some remarkable results will be summarised in the following pages (sections 3 to 5).

Besides getting new insight into tip clearance flow configurations, our study was also meant to provide input and validation data for CFD simulations. A number of computations have been carried out and compared to the wind tunnel tests described hereafter: unsteady RANS [6], LES [7], ZLES [8]-[9] and LBM [24] techniques have been tested on the tip clearance configuration described hereafter. Therefore some benchmarking issues will be underlined and a few numerical results will also be shown in order to illustrate its benchmarking capacity but for the sake of conciseness, this lecture will be focused on experimental issues and results.

2.0 EXPERIMENTAL SET-UP

2.1 Over-all set-up

All the measurements are carried out in the ECL anechoic wind tunnel that opens into a $10\ \text{m} \times 8\ \text{m} \times 8\ \text{m}$ anechoic room. The subsonic flow is guided into the room by an $0.56\ \text{m} \times 0.56\ \text{m}$ square 2 m long duct, accelerated through an $0.45\ \text{m} \times 0.2\ \text{m}$ nozzle as a $70\ \text{m/s}$ jet flow. The resulting rectangular jet flow is confined between 2 horizontal plates that are 0.2 m apart in the spanwise direction of the airfoil that is hold by the upper plate and the airfoil is located about 1.5 chord downstream of the nozzle in the potential core of the jet, in agreement with recommendations given in Lecture n°1. An adjustable gap h is maintained between the airfoil lower end (tip) and the lower plate (casing). In order to obtain a significant tip leakage flow without relative motion between the airfoil and the wall, the airfoil is heavily loaded. This is achieved by choosing a significantly cambered thick airfoil (NACA5510 with: chord $c = 200$ mm, span ℓ such that $\ell + h = 200$ mm, and maximum thickness $e = 20$ mm) at a high angle of attack. In fact the jet is deviated by the airfoil, which has two consequences: the first is that the "effective" angle of attack (eAoA= 7.5°) is about half the geometric (AoA =15°); the second is that the jet is prone to hit the anechoic treatment of the room, damaging the wedges. To avoid this, the rectangular duct is connected to a 7.5° bend near the rear wall of the chamber. This has been discussed and sketched in the first introductory lecture. The sketch of the inlet

duct is recalled on Fig 2-1 hereafter, whereas the test section is illustrated and sketched on Fig 2-2.

There have been two sets of campaigns, one in the context of the aforementioned EU project PROBAND (hereafter referred to as phase 1), the other as part of a Sino-French project AXIOOM about tip and corner flows in turbomachines (hereafter referred to as phase 2). Slight changes have been operated between the two phases in order to better isolate the tip noise contribution from other sources during the second phase.

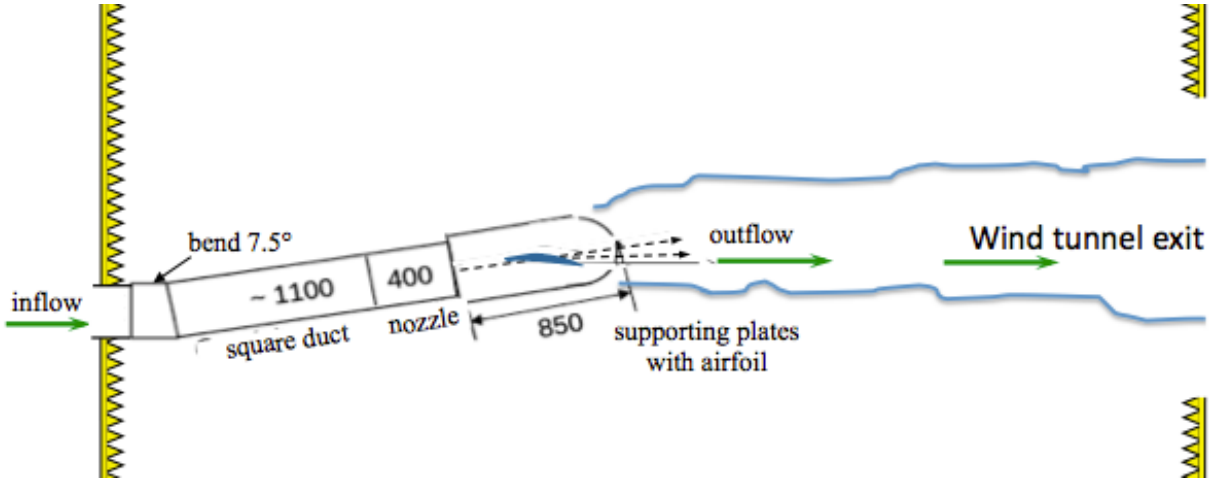

Fig 2-1: schematic view of the experiment showing the bend

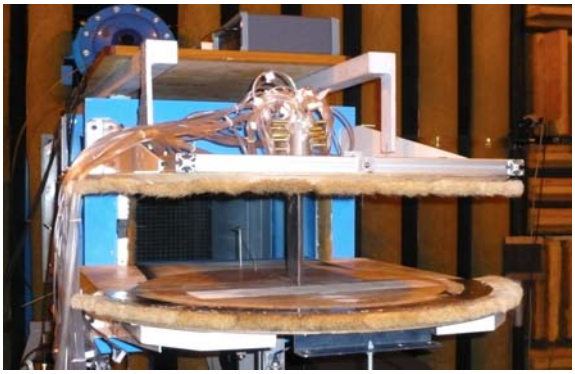

Picture of the experimental set-up, where the airfoil is equipped with static pressure probes and an HWA probe is in an upstream section

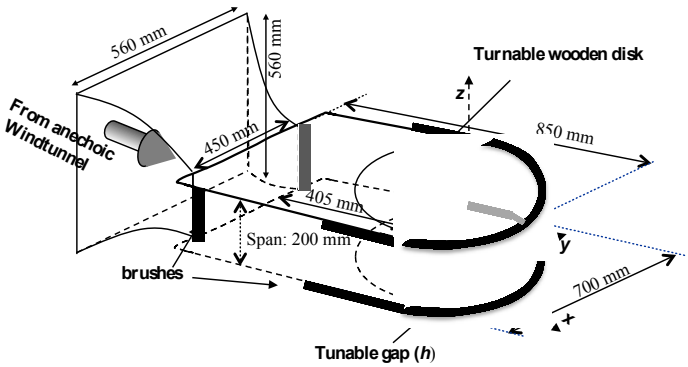

Sketch showing the coordinate system. The dark stripes symbolise the brushes that reduce the outer shear layer noise. The tip leakage gap is located between the airfoil tip and the lower plate

Fig 2-2 Experimental set-up: view of test section and coordinate system

2.1 Measurements

Among the multiple measurement techniques that have been applied during these test campaigns, Hot Wire Anemometry (HWA), Laser Doppler Velocimetry (LDV), Particle Image Velocimetry (PIV), both classical and Time Resolved (TR) were used for the characterisation of the velocity field. Moreover, both steady and unsteady wall pressure measurements have been carried out, not only on the airfoil but also on the casing plate. Far field measurements were also performed.

Details about the various measurement set-ups can be found in a few dedicated papers for the two sets of experiments [3]-[5]. Note that the two component TR PIV was conducted with the camera facing the flow, which was a particular challenge since the vaporised glycerine condensed on the lens that had to be cleaned

every 5000 snapshots. This installation allowed measuring the Tip Leakage Vortex (TLV) in sections located upstream of the Trailing Edge (TE) due to the camera position and the Laser source placed on the aft port side of the flow. The 3 component TR-PIV could be carried out without "wetting" the lenses due to the 45° angle each camera made with the normal-to-flow direction but as a tribute, light reflections by the airfoil had a stronger impact: therefore, measurements were restricted to a plane located slightly downstream of the TE, the light source being placed under the casing plate equipped with a glass window.

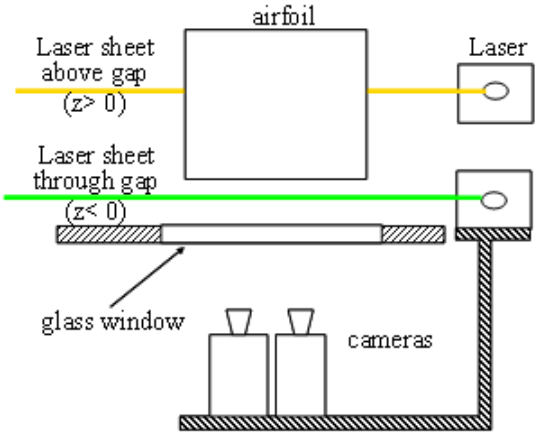

2 component "classical" PIV in the gap

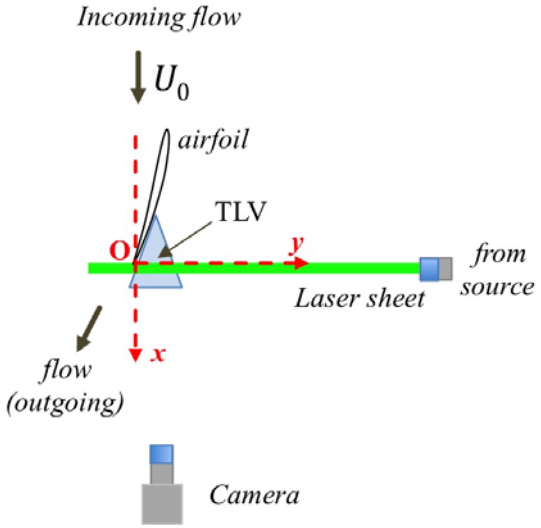

2 component TR PIV of Tip Leakage Vortex (TLV)

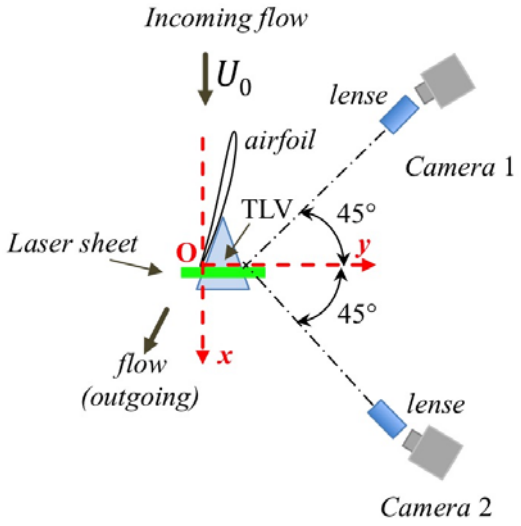

3 component TR PIV of Tip Leakage Vortex (TLV)

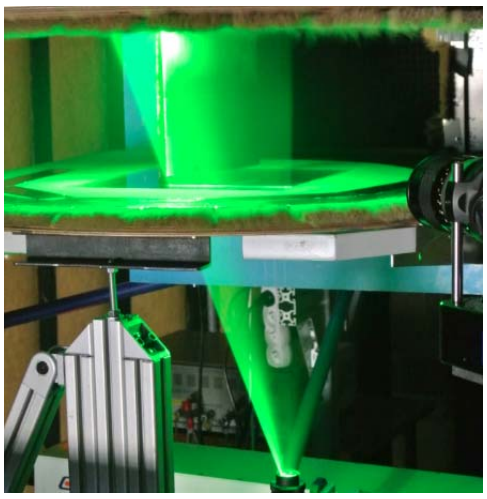

3 component TR PIV of Tip Leakage Vortex (TLV): view of the cameras and the Laser sheet

Fig 2-3: PIV set-ups and photographs

Unsteady wall pressure measurements were carried using remote microphone probes (see Fig 2-4 middle) with *in situ* calibration (see Fig 2-4 bottom plot) as described by M. Roger in Lecture n°3 of the present series. On the top right plot of Fig 2-4, the lines that are recognisable on the airfoil correspond to the locations of the embedded capillary tubes. The top left plot sketches only 20 probes located on the very tip, the suction side near the tip and the trailing edge out of 56 wall pressure probes distributed over and beneath the airfoil.

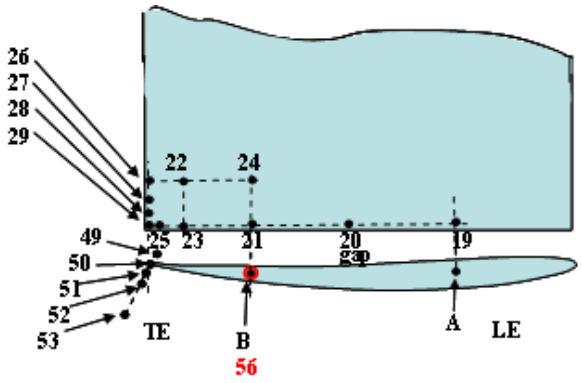

Sketch of main pressure probes

Photograph of airfoil equipped with pressure probes. Impact of laser sheet can also be seen

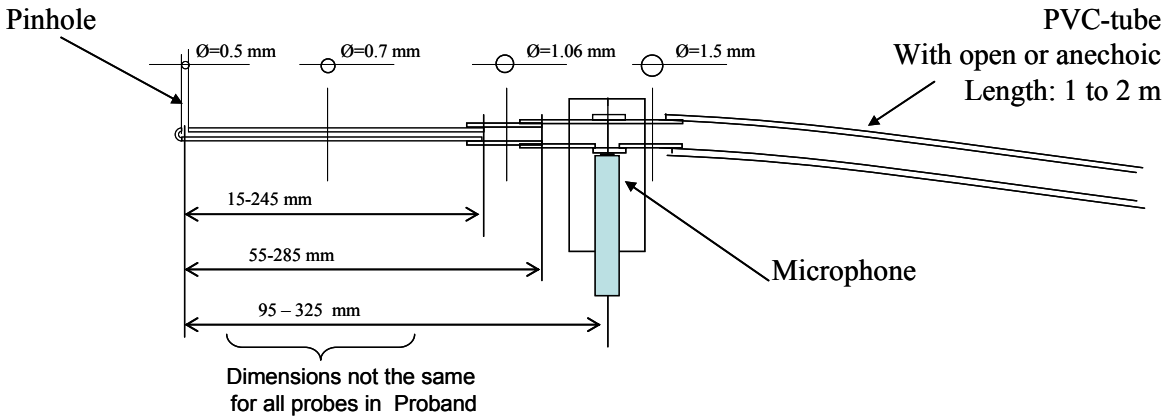

Sketch of the remote pressure probes

In situ calibration of the remote probes: amplitude, phase an coherence of transfert function

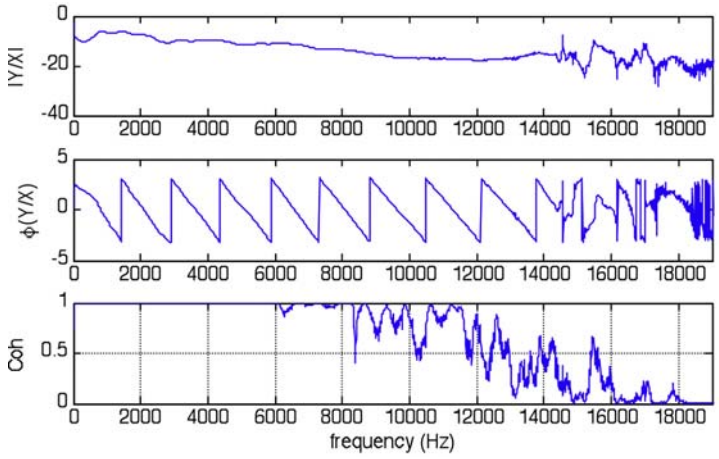

Fig 2.4: Wall pressure measurements with detail of the probes, the tip and tip trailing edge corner

2.2 Coordinates

Most results are shown in a Trailing Edge (TE) based coordinate system whose origin O is located on the trailing edge/gap corner (see Fig. 2). The $x-$ axis is aligned with the main flow direction, that is the nozzle axis, the $z-$axis is in the spanwise (vertical) direction and is oriented from the lower to the upper plate whereas the $y-\ axis$ is in the cross-stream direction to the left looking into the streamwise direction.

2.3 Reference configuration

Although many parameters haven been varied (flow velocity U_0, tip gap h, angle of attack AoA…) most results were obtained in the following reference configuration: $U_0 = 70$ m/s; $h = 10$ mm; $AoA = 15°$. This corresponds to a Mach number $M\sim 0.2$ and a chord-based Reynolds number $Re \approx 930\,000$. The reference plane for the PIV measurements parallel to the tip gap was the mid gap section (z= -5 mm). The TR-PIV was conducted in several normal-to-flow sections, mostly in the $x = 2$ mm plane (2 mm downstream of the TE).

3.0 MEAN FLOW & TIP VORTEX

3.1 Mean pressure and velocity field

The flow is uniform within 0.6% and its turbulence level in the main flow at the jet nozzle is $u'/U_0\sim 0.5\%$. During the first phase it was about 0.8%. For a $U_0 = 70$ m/s nozzle outlet velocity, the boundary layer thickness of the second set of campaigns is $\delta\sim 7.5$ mm half a chord upstream of the airfoil instead of 18 mm during the first phase. Similarly, the displacement thickness is reduced from $\delta^*\sim 1.4$ mm to 0.95 mm.

The main boundary layer parameters extracted from the profiles plotted on are summarised in Table 1:

	$x = -5c/2$	$x = -2c$	$x = -7c/4$	$x = -3c/2$
δ (/mm)	4.5	6.2	7.0	7.5
δ^* (/mm)	0.56	0.83	0.91	0.95
Θ (/mm)	0.35	0.45	0.50	0.56
H	1.62	1.84	1.82	1.70

Table 3-1: Summary of main boundary layer parameters upstream of the airfoil distance are given from the trailing edge. Boundary layer thickness δ, displacement thickness δ^* momentum thickness θ and shape factor H. ($U_0 = 70$ m/s; $h = 10$ mm, $\alpha = 15°$)

The data of Table 3-1, along with the inlet profiles and the pressure distribution at mid-span are required for CFD inlet conditions and tuning: indeed some simulations model the whole experimental set-up, including the semi-open jet [8];[24], whereas others create equivalent flow conditions with a uniform flow throughout the domain [6]-[7]. In the latter approach, the equivalent angle of attack has to be tuned by maximising the fit with the experimental pressure coefficient. For full simulations, the experimental pressure coefficient serves as an *a posteriori* validation only.

Fig 3-1 illustrates these inflow and mean pressure validations in the case of a ZLES simulation of the second configuration. [7]-[8]. It is interesting to note that the mean velocity fits almost perfectly with the experiment whereas the rms values do not. The CFD turbulence profiles are much sharper and narrower than the experimental ones, indicating for a possible lack of diffusion in the CFD. An additional factor might be the background noise of the LDV measurements that would explain the relatively high fluctuation levels far from that wall.

Similarly, the computed and measured pressure coefficients compare relatively well, considering the fact that

this quantity is sensitive to slightest flow differences. However, the maximum pressure coefficient at mid span is somewhat underestimated by the computation (no fitting has been operated here since the simulation encompasses the whole jet flow with the plates and the ambient fluid at rest. The strong suction at half chord along the airfoil tip corresponds to the position where the tip jet is expelled from the clearance and entrains fluid from its vicinity.

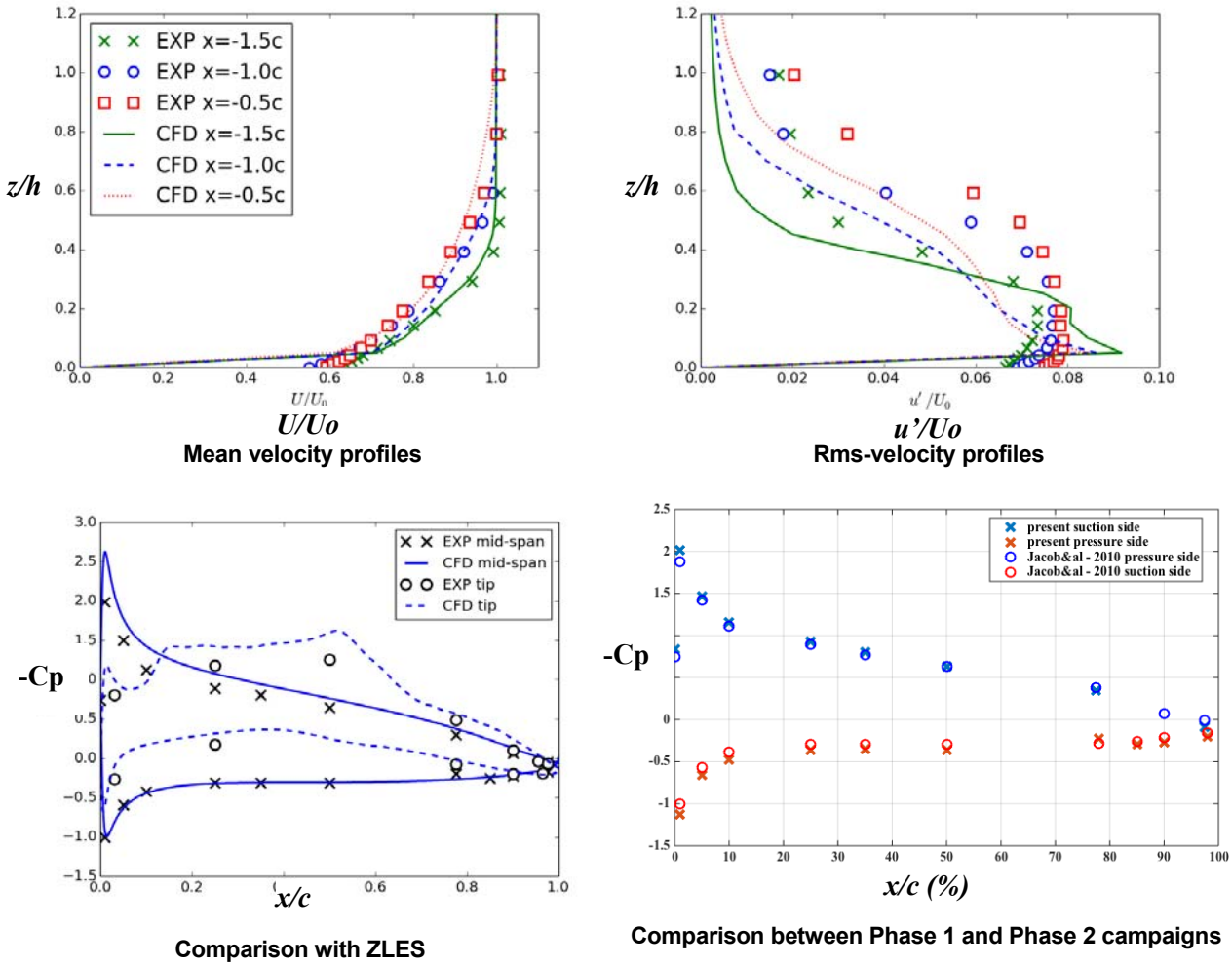

Pressure coefficient $-C_p$ at mid spand and alon the tip

Fig 3-1 Velocity profiles and pressure coefficient at airfoil mid-span: measurement/ZLES ($U_0 = 70$ m/s; $h = 10$ mm, $\alpha = 15°$)

Similar results (not shown here) have been obtained for the first configuration with a LBM computation: the results fit much better to the experimental data [24]. The bottom right plot of Fig 3-1 shows the good agreement of the airfoil loading between the phase [3] and the phase 2 of the experiment [4]-[5].

3.2 Tip Leakage Vortex (TLV) characterisation

The characterisation of the TLV is one of the issues of this experiment. During the first phase, the trace of the TLV in planes parallel to gap allowed for measurements in the tip gap, but only showed longitudinal cross-sections of the vortex (Fig 3-3).

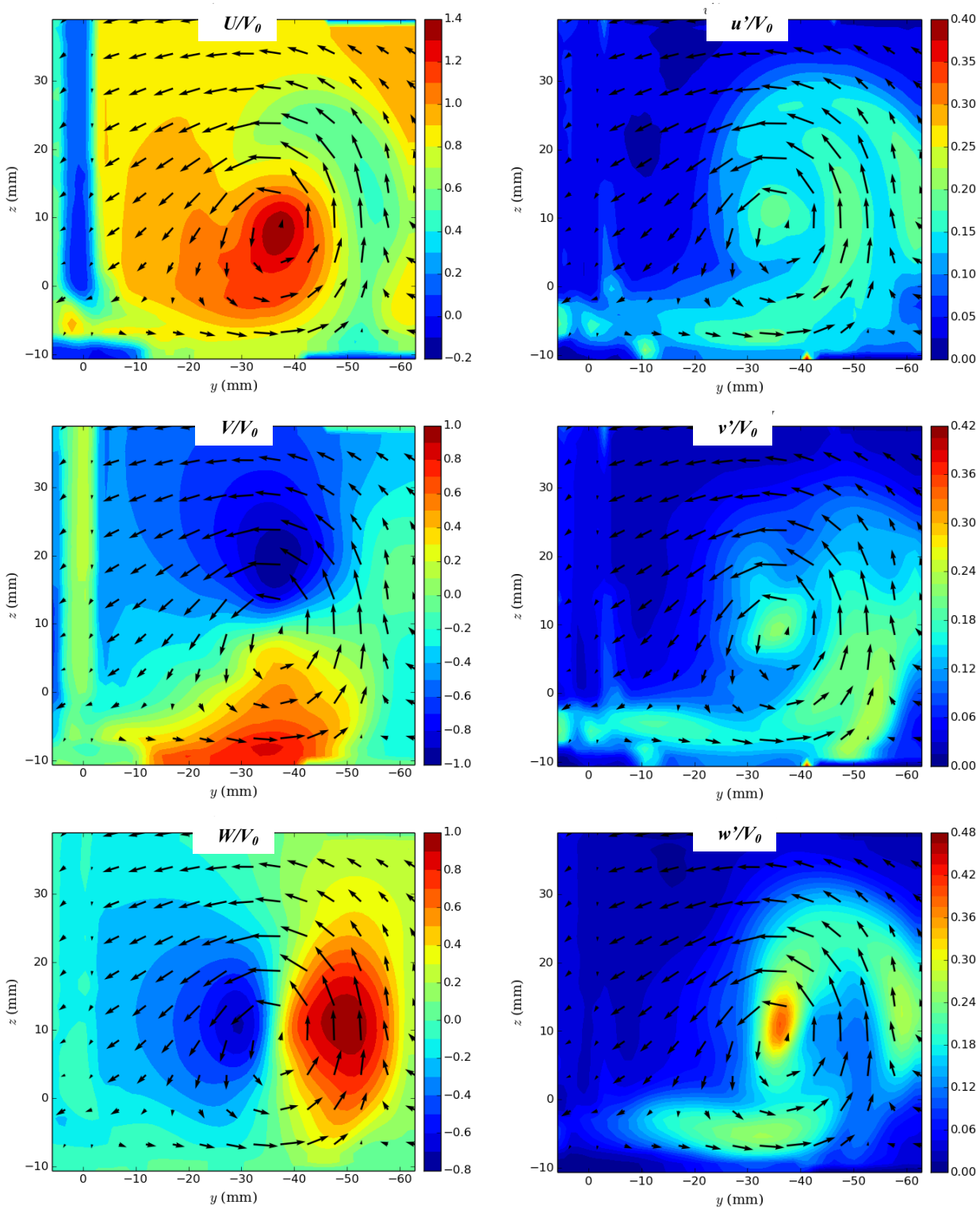

Fig 3-2 Mean and rms values of the 3 velocity components in downstream of the TE ($x = 2$ mm) showing a typical cross-stream section of the TLV. Arrows represent the mean velocity vectors in the cross-stream plane. View into the upstream direction: the influence of the airfoil TE can be seen on the left (near $x = 0$) ($U_0 = 70$ m/s; $h = 10$ mm, $\alpha = 15°$)

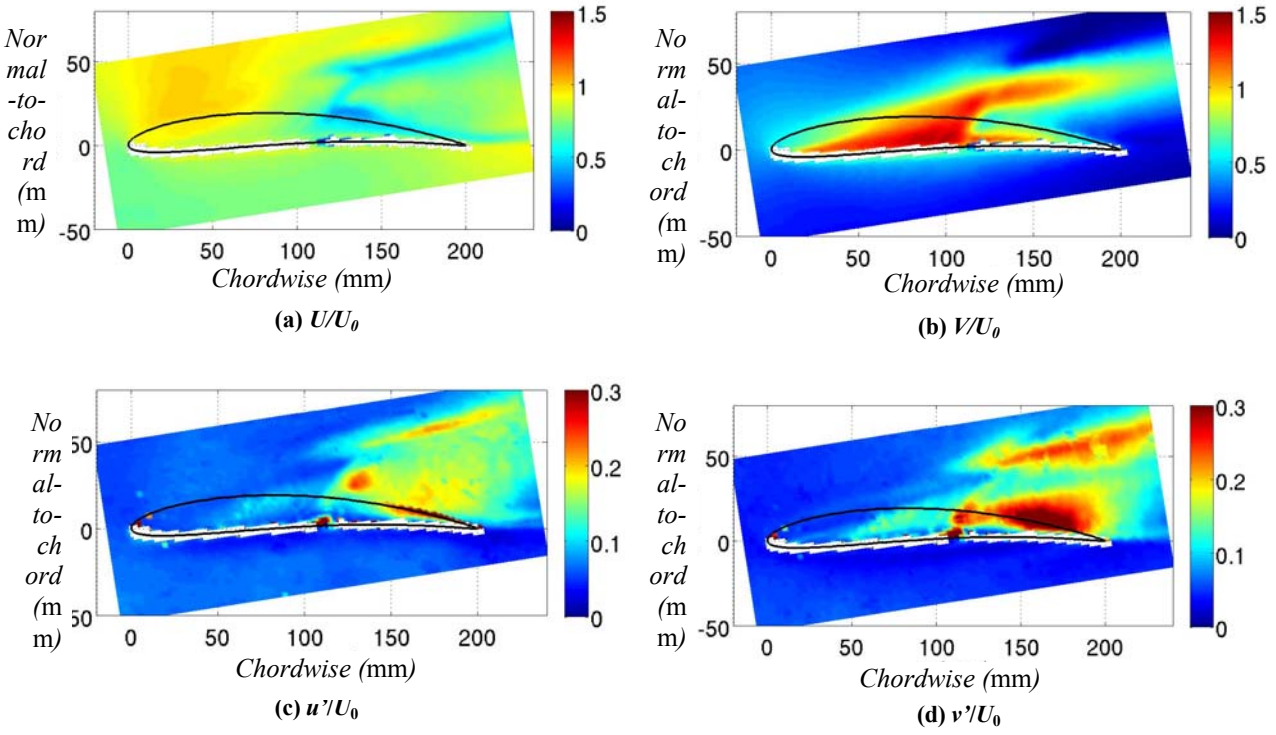

Fig 3-3 Mean and rms values of the streamwise and cross-stream velocity in the gap plane ($z = -3$ mm): for these measurements from the first phase, co-ordinates are built on the chord and originate the leading edge ($U_0 = 70$ m/s; $h = 10$ mm, $\alpha = 15°$)

Fig 3-2 shows the characteristic structure of the clockwise TLV as seen from a downstream point (which explains why it appears as clockwise): higher fluctuations are observed in the outer region of the TLV where it carries flow disturbances from the casing boundary layer and undergoes strong shear with the outer flow associated to a deceleration. On fig 3-3, the development of this slowed shear layer as well as another shear region between the downstream suction side and the TLV appears very clearly. The remarkable feature of Fig 3-3 is the jet-like structure of the cross-flow that pushes fluid from the pressure side to the suction side feeding the TLV. This cross flow also explains the strong suction observed at mid-chord on the blade near the suction side tip edge (see Fig 3.1).

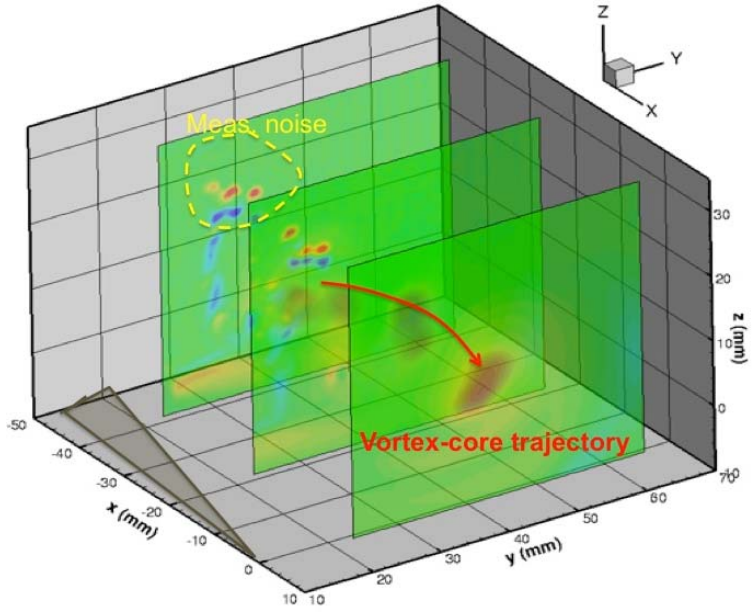

Fig 3-4 TVL roll-up in 3 cross sections obtained from 2D-2C PIV: $x = -40; -20$ and $+2$ mm the trace of the airfoil on the casing plate is shown on the left part of the plot in dark grey. The mean streamwise vorticity component is plotted; red corresponds to anti-clockwise and blue to clockwise rotation. The spots surrounded by a yellow circle correspond to measurement noise.

A view of the streamwise mean vorticity in several cross-stream sections (3 PIV planes) is plotted on Fig 3-4. The red arrow qualitatively indicates the vortex trajectory. This figure completes the picture given by Figs. 3-2 and 3-3. It can be seen that the vortex is almost parallel

to the $x-$ direction, that is, it roughly follows the direction of the upstream flow. It shows the growth of the vortex as it is convected into the downstream direction. However, in order to obtain a better estimate of the vortex core and size, further post-processing tools are required.

3.2 TLV mean vorticity and NAM

In order to better characterise the TLV and its mean trajectory, several physical quantities are computed throughout the TLV cross-section: the streamwise vorticity ω_x, the circulation across the TLV, and two measures based on the concept of Normalised Angular Momentum whose definitions are briefly recalled hereafter. These two measures are given as functions Γ_1 and Γ_2 by Michard *et al.*[25] and Graftiaux *et al.*[26] that are suited to identify the vortex centre and its extent respectively. They consider only the topology of the velocity field and smooth out the small-scale turbulent intermittency.

The vortex centre identification function Γ_1 at a fixed point P is defined as the NAM based on the absolute velocity as follows:

$$\Gamma_1(P) = \frac{1}{S}\int_{M\in S} \frac{(PM \wedge U_M)\cdot \mathbf{x}}{||PM||\cdot||U_M||}\, dS$$

where S is a 2D area surrounding P and $\mathbf{x}$ is the unit vector normal to the plane (here the streamwise direction). $|\Gamma_1|$ is a dimensionless scalar bounded by 1. This bound is reached at the vortex centre. The sign of Γ_1 indicates the direction of its rotation and appears as the absolute NAM.

Similarly, the vortex boundary identification function Γ_2 is derived from the relative velocity field, by taking into account a local mean convection velocity $\widetilde{U}_P$ around P:

$$\Gamma_2(P) = \frac{1}{S}\int_{M\in S} \frac{[PM \wedge (U_M - \widetilde{U}_P)]\cdot \mathbf{x}}{||PM||\cdot||U_M - \widetilde{U}_P||}\, dS$$

where $\widetilde{U}_P = \frac{1}{S}\int_S U\, dS$. Thus Γ_2 appears to be a relative NAM.

Since the velocity field of the PIV measurements is sampled at discrete spatial locations, the two functions are approximated in the post-processing by

$$\Gamma_1(P) = \frac{1}{N}\sum_S \frac{(PM \wedge U_M)\cdot z}{||PM||\cdot||U_M||}$$

$$\Gamma_2(P) = \frac{1}{N}\sum_S \frac{[PM \wedge (U_M - \widetilde{U}_P)]\cdot z}{||PM||\cdot||U_M - \widetilde{U}_P||}$$

where N is the number of points M inside S.

According to refs.[25]-[26]the vortex core region is bounded by the contour $\Gamma_2 = 2/\pi$.

Both functions act as a small filter by removing small size eddies. The number of points $N = 7$ to 9 are found to be a good compromise between the filter size and the precision of the vortex characterisation for the mean field. A smaller number is more appropriate for characterising instantaneous vortices. On Fig 3-5, the different vortex characterisation tools are illustrated for the mean TLV flow field in the $x = 2$ mm plane.

The vorticity (plot (a)) does not provide precise information about the vortex centre (orange spot) whereas the maximum values of the Γ_1 (dark red spot on plot (c)) locate the centre in a narrow region, the very centre being marked by a small white cross. The maximum can be determined more precisely as shown on Fig 3-6. As for the circulation (Fig 3-5 plot (b)), its maximum roughly estimates the TLV core radius (the decrease is due to the neighbouring counter-rotating secondary vortex). Conversely, the vortex core size and shape are vey well predicted by Γ_2 (note that the value $2/\pi \sim 0.64$ is not easy to distinguish on Fig 3-5 plot (d): therefore the corresponding iso-contour is plotted on Fig 3-6 along with iso-contours of Γ_1 (the maximum is shown by a white cross) on a colour map of the 2D mean velocity modulus with mean velocity vectors. It is interesting to note that the region where the 2D velocity vanishes also provides a good idea of the vortex centre location.

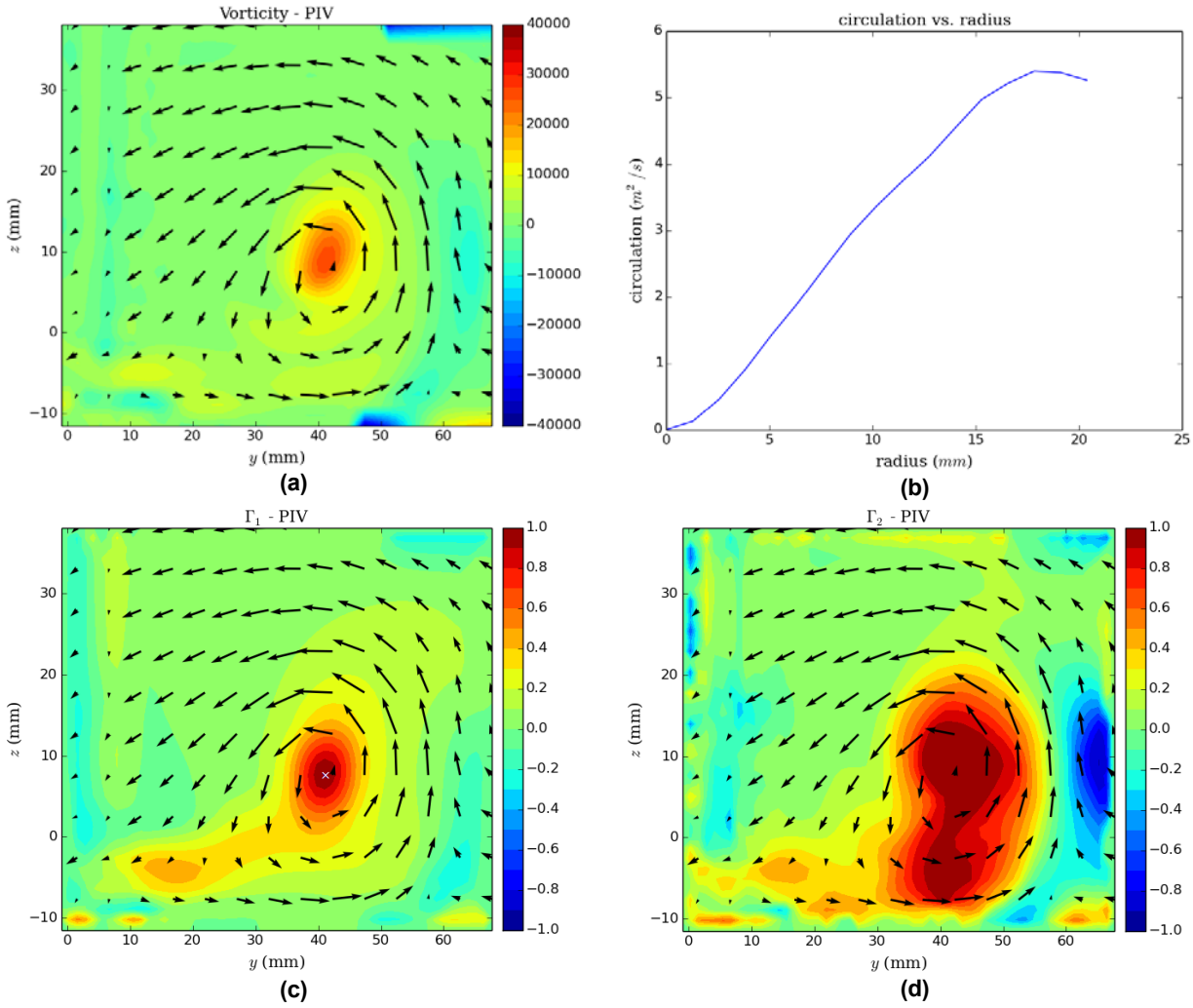

Fig 3-5: Vortex characterization. From left to right and from top to bottom: mean streamwise vorticity ω_x, Circulation, Γ_1, Γ_2. ($U_0 = 70$ m/s; $h = 10$ mm, $\alpha = 15°$)

Similarly, the vortex characterisation can be carried out in the other PIV planes (x=−20 mm and x=−40 mm). The TLV centre location found in the 3 planes is plotted on figure 3-6. A cross-section of the airfoil as well as the TLV centre computed in a similar manner from LES and RANS data [6]-[7], are also plotted on Fig. 3-6 (d). Very good agreement is found between the PIV, LES and RANS predictions of the TLV trajectories. It can also be seen that these trajectories are between the chord and the mean flow direction.

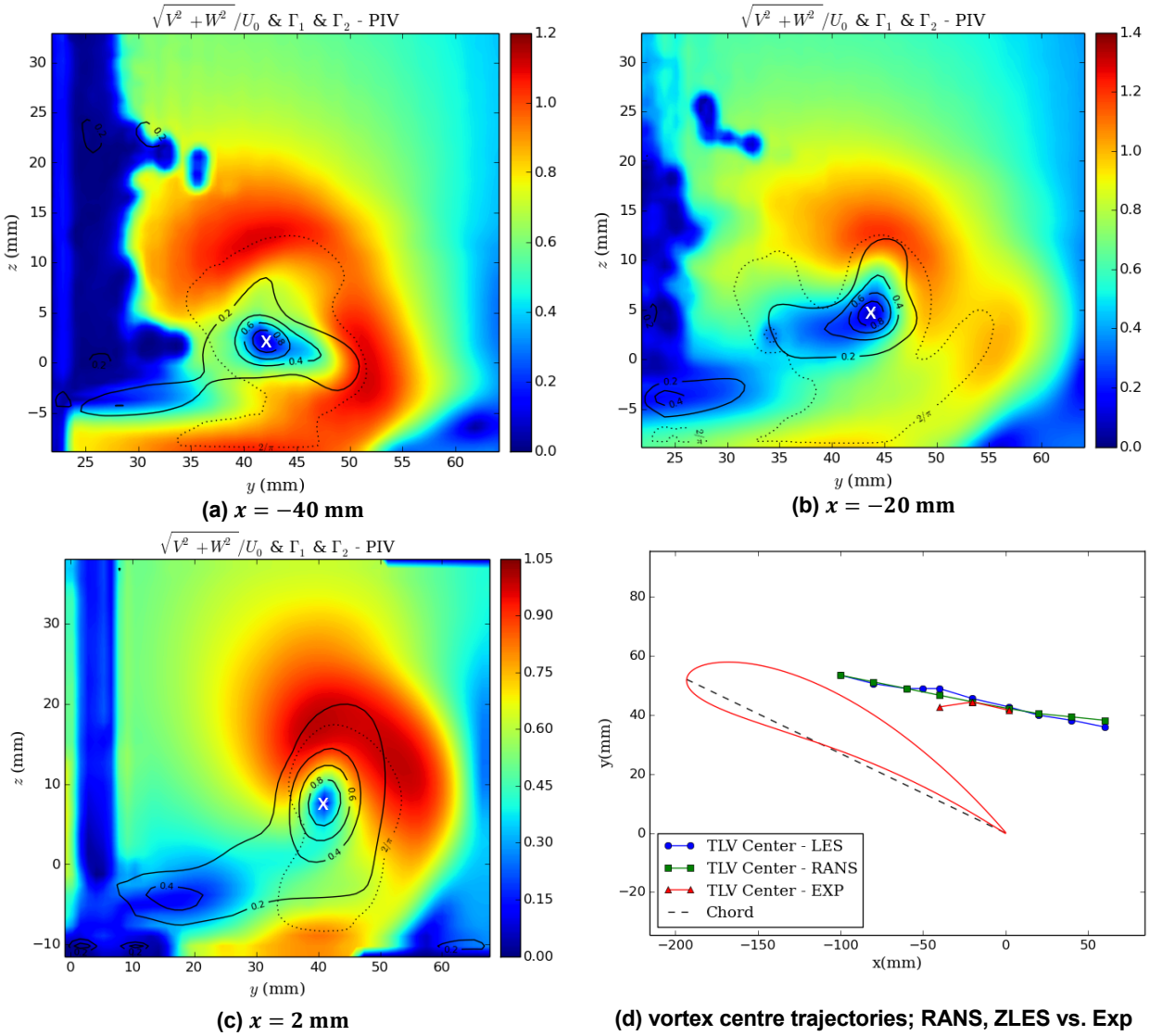

(a) $x = -40$ mm

(b) $x = -20$ mm

(c) $x = 2$ mm

(d) vortex centre trajectories; RANS, ZLES vs. Exp

Fig 3-6 Iso-contour $\Gamma_2 = 2/\pi$ (dashed line), iso-contours of Γ_1 (continuous lines, maximum indicated by a cross) and colour map of the non-dimensional 2D mean velocity modulus $\sqrt{V^2+W^2}/U_0$ obtained from 2D-3C TR-PIV data in 3 streamwise planes. Comparing mean trajectories of simulations against the experiment. ($U_0 = 70$ m/s; $h = 10$ mm, $\alpha = 15°$)

4.0 THE UNSTEADY TIP CLEARANCE FLOW

As pointed out in the introductory lecture, unsteady flow features are the crucial for aeroacoustics.

4.1 Tip vortex oscillations

The vortex centre detection method is here applied to the instantaneous velocity fields from the TR PIV measurements to be related to the oscillations of the TLV, also known as vortex wandering. In order to highlight possible TLV oscillations (suggested in the introduction), the vortex centre locations are computed in time domain using the Γ_1 function. The probability density function (pdf) of the vortex centre location is computed in each PIV plane as shown on the left plot of Fig. 4-1 for the $x = 2$ mm plane (near the TE).

The width of the TLV central region (where the pdf is highest) is about 3 mm, far above the PIV spatial resolution. Similarly, the height of this region is about 2 mm, both being above the PIV resolution that is

about 0.8 mm. However, the size of the region depends on the size of the control surface (number of velocity points) chosen for the Γ_1 as shown on the right plot of Fig. 4-1. As argued in the previous section, the number of points for relevant Γ_1 estimates should not be too large ($N < 10$ or even less typically) and in the present case, the decrease of the amplitude reported on the right plot of Fig. 4-1 is also due to the influence of the neighbouring vortical structures (secondary vortex etc.) when the integration region (number of points) increases. To conclude, TLV oscillations occur indeed but reach small amplitude compared to the TLV size.

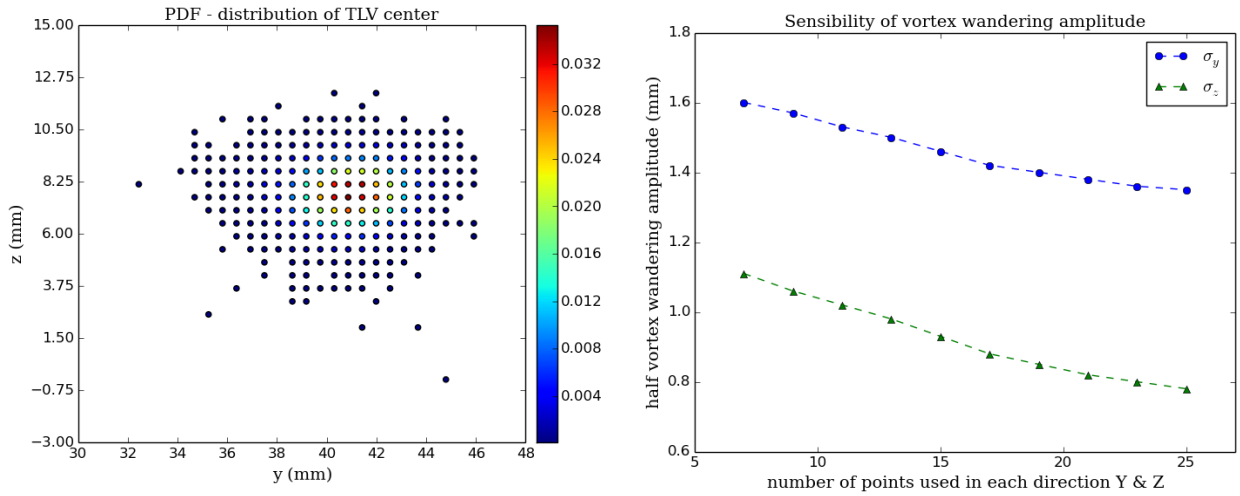

Fig 4-1: probability density function of the vortex centre positions in the $x = 2$ mm plane (left) dependence on the integration size taken for Γ_1 (right). ($U_0 = 70$ m/s; $h = 10$ mm, $\alpha = 15°$)

4.2 Wall pressure spectra

On Fig 4-2 typical spectra from the suction side on the tip edge are traced on plot (a). Plot (b) is obtained by probes located in and nearby the tip clearance at $x/c = 0.775$. A hump between 0.7 and 3 kHz typically can be recognised on most spectra, even at the pressure side tip edge (probes 46). Similar features are also found on velocity spectra in this region and the hump corresponds to that found in the outer shear layer. This confirms the scenario of the roll- up mechanism: perturbations generated in the gap at ¾ chord are expelled from the gap and convected to the outer shear layer of the tip vortex. The relatively high broadband level of the velocity spectra, which is not obvious in the gap pressure spectra, is probably due to turbulence from the casing wall boundary layer entrained by the tip vortex. The maximum of the wall pressure hump lies about 1.4 kHz, which corresponds to a chord based Strouhal number St_c about 4. It is however not so clearly recognisable upstream of the tip jet (probe 19) and it extends to very high frequencies for probe 21 that is located just above the upper shear layer of the tip jet where it leaves the gap. This shear layer can possibly be accounted for additional higher frequency perturbations: the frequency range comprised between 4 and 7 kHz corresponds to a gap based Strouhal number $\mathrm{St}_h = fh/V_{max}$ (where V_{max} ~100 m/s is the tip jet velocity) that varies between 0.4 and 0.7 which somewhat high for mixing noise sources. In [27] similar results are found for small gaps down to $h = 3$ mm (h/c~0.15). For $h < 3$ mm the hump disappears and the pressure perturbations become very small inside the gap, whereas for $h > 10\,mm$, the perturbations become independent from the gap which means that the influence of the casing wall vanishes. On plot (e) of Fig 4.2, a comparison with ZLES results is shown [9]: the agreement is excellent for the pressure side edge probe at $x = 0.775\ c$ (n°46) and fair for the corresponding suction side probe (n°21).

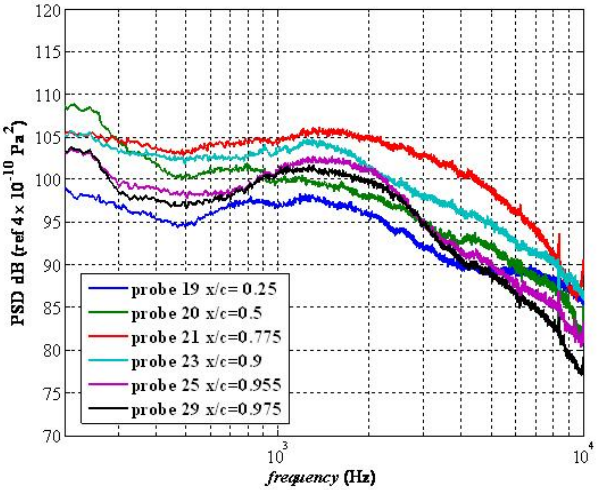

(a)

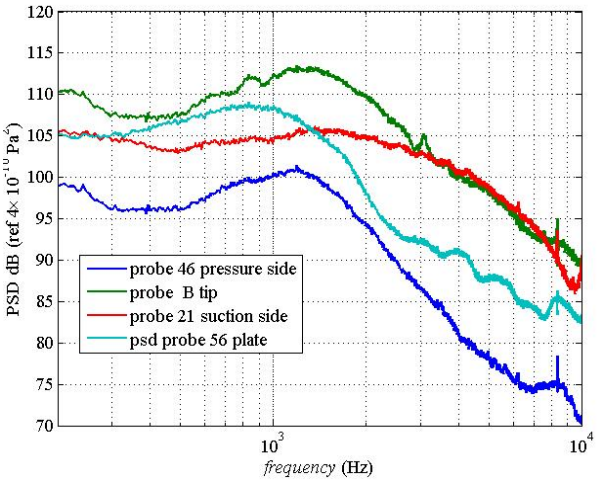

(b)

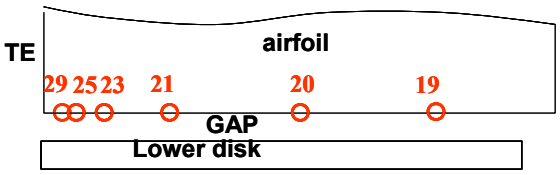

(c)

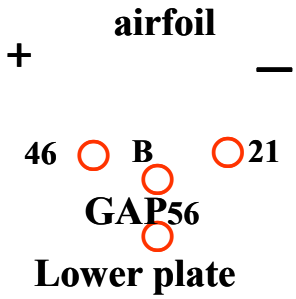

(d)

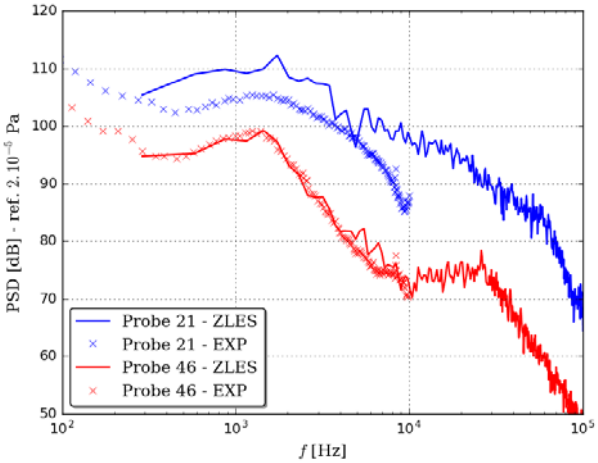

(e)

Figure 4.2: Wall pressure spectra in the tip region: (a) along the tip suction side at various chord-wise positions sketched in (c); (b) in the gap at $x/c = 0.775$ at various points sketched in (d) – (e): comparison with ZLES. ($U_0 = 70$ m/s; $h = 10$ mm, $\alpha = 15°$)

4.3 Coherence wall pressure – velocity

Coherence highlights a linear link between flow phenomena that are causally linked, that is, originating from a common physical mechanism. This link is established as a function of frequency and can be interpreted as a correlation spectrum. The coherence $\gamma^2_{x,y}$ between two signals x and y is defined as the non-dimensional cross-spectrum :

$$\gamma^2_{x,y}(f) = \frac{|S_{x,y}(f)|^2}{S_{x,x}(f)S_{y,y}(f)}$$

Its value is comprised between 0 (incoherent signals) and 1 (fully coherent signals). We show successively two unusual applications of the coherence function.

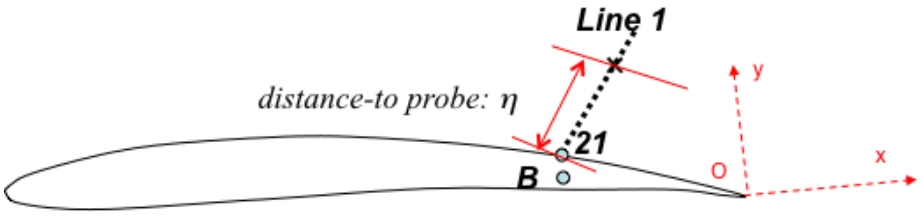

(a) Sketch of the probe position for LDV- wall pressure coherence

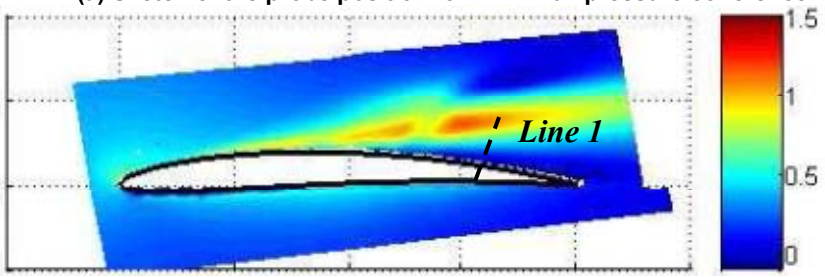

(b) Plot showing the position of Line 1 with respect to the turbulent sjear layer in the probe plane ($z = 0$)

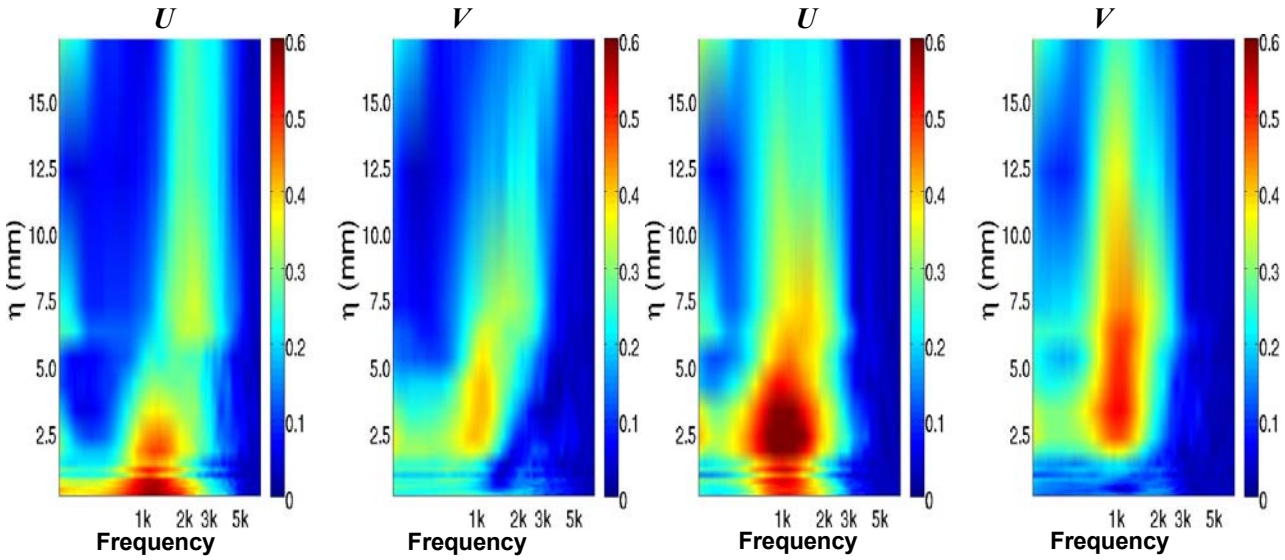

(c) Line 1 – probe 21 coherence

(d) Line 1 – probe B

Fig 4-3 Coherence: LDV measurement point moves along line 1 - correlated to unsteady pressure probe 21 ($x = 0.775c$, $z = 1$ mm above the tip edge on the suction side) or to the unsteady pressure probe B (on tip at $x = 0.775c$). ($U_0 = 70$ m/s; $h = 10$ mm, $\alpha = 15°$)

On Fig 4-3, the coherence between two components of the velocity obtained by LDV measurements along a

line (line 1) and the signals obtained successively by two wall pressure probes are mapped: the colours indicate levels of coherence (up to 0.6) whereas the two axes are the frequency and the distances between the velocity probe and the pressure probe respectively.

It should be noted that Line 1 crosses the TLV highly turbulent shear layers near the wall as shown on plot b of Fig 4.3. The maps of Fig 4.3 show that the turbulence in the TLV, especially in the outer shear layer where the TLV meets the outer flow, is actually coherent with the wall pressure. Since the flow moves from the gap to the outer region, this means that the turbulence in the outer region actually originates from the gap as mentioned in the previous section.

The other remarkable conclusion is that although the governing mechanisms of this flow are rather of broadband nature, and are thus expected to be only weekly correlated in space, the coherence levels found here are quite significant, not to say very high. Thus the tip leakage flow appears to generate coherent structures in medium range frequencies from 0.5 up to 2.5 kHz. This corresponds to the frequency range of the spectral hump observed in the wall pressure spectra.

Let us now examine another aspect of velocity- wall pressure coherence: the wall pressure probe is chosen at the upstream part of the tip leakage jet (probe n°19) and a single Hot Wire Anemometry (HWA) Probe is moved approximately in the direction of the incoming flow, that is, along the TLV, starting at a distance of 1 mm from the wall pressure probe and moving 20.5 mm downstream. The right plot of Fig 4-4 sketches the wall pressure probe location and the successive HWA probe positions. Results are shown on the left plot of this figure. For all probe positions a medium frequency hump is observed that is centred on frequencies comprised between 0.7 kHz and 1.3 kHz. For the two HWA positions that are immediately at the tip edge, where the tip leakage jet leaves the gap, another hump is observed at much higher frequencies (about 6 to 7 kHz). This frequency seems to be associated to the tip jet.

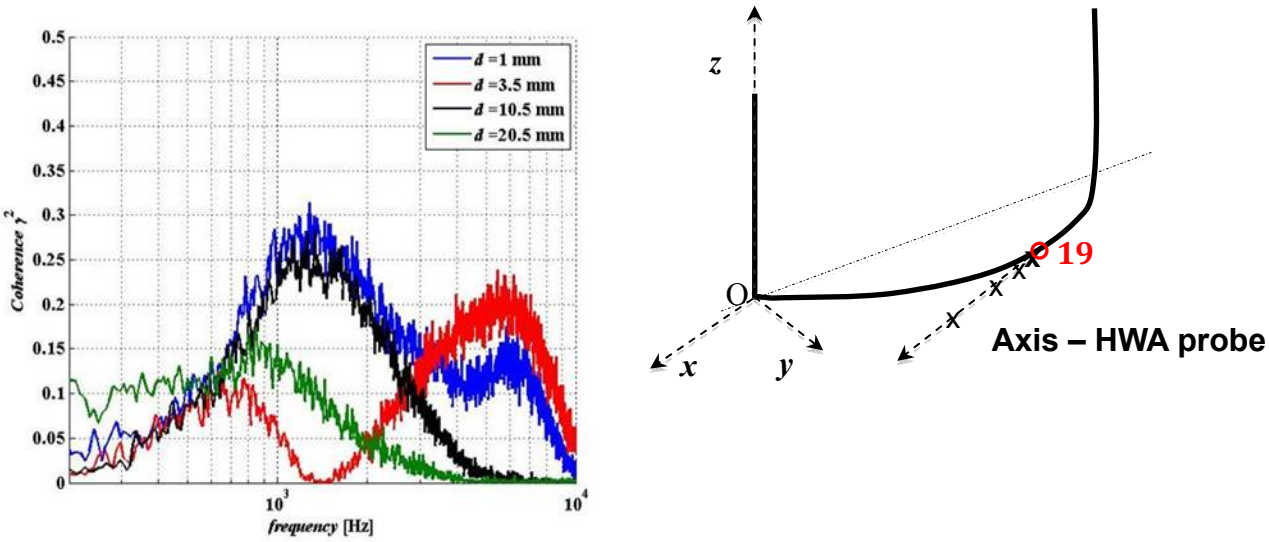

Fig 4-4 : HWA coherence with a probe (n°19) located at the upstream part of the Tip gap jet $x = 0.25\,c$: The hot wire positions follow a line that corresponds to the mean flow direction ($U_0 = 70$ m/s; $h = 10$ mm, $\alpha = 15°$)

4.4 Wavelet Analysis

The wavelet analysis has many common points with a Fourier analysis, the main differences are that a family of wavelets (the Battle-Lemarie wavelets in the present study) replaces the complex exponentials. The

wavelet transform of a signal p writes:

$$w(r,t) = C_\psi^{\frac{1}{2}} \int p(\tau)\Psi^* \left(\frac{t-\tau}{r}\right) d\tau$$

where $C_\psi^{\frac{1}{2}}$ is a normalization coefficient and * denotes the complex conjugate. The result of a decomposition on this family of transient functions are wavelet coefficients that depend both on time and on a time scale r (the time scale of the wavelet) whose inverse $1/r$ is the wavelet equivalent of the frequency. On the basis of this wavelet transform, it is possible to carry out cross-wavelet analyses in order to correlate wavelets from 2 signals. The purpose of using wavelets is to obtain a sharper description of transient flow phenomena (e.g. coherent structures in turbulent flows such as turbulent boundary layers). In particular the LIM (local intermittency measure) and its two-signal counterpart, the cross-LIM, generalizes the concepts of energy and cross-spectrum respectively.

$$LIM = \frac{|w(r,t)|^2}{\langle |w(r,t)|^2 \rangle_t}$$

Peaks of *LIM* represent large contributions of a signal's variations to its overall power level. Therefore the *LIM* amplitude at a selected scale r can be thresholded in order to select events responsible for the largest fluctuations of the analysed signal and to determine how they are distributed in time. Once the events have been selected and localized in the time, a conditional average of the original signal is performed. This auto-conditioning procedure leads to an ensemble-averaged time signature of the fluctuations, which represents the most probable shape of the most energetic structures that are hidden in the original chaotic signal. The original method was introduced in 1997 by Camussi and Guj [28]. The example shown here is obtained from simultaneous PIV/pressure measurements performed in the reference configuration. The conditioning method explained above is applied to the PIV/wall-pressure data: firstly, aerodynamic events correlated to large localized pressure peaks at the wall of the airfoil are detected. Secondly, the conditional average is performed on those PIV snapshots that are acquired simultaneously with the selected pressure events. An example of this approach is shown on Fig 4-5 where a snapshot is shown on plot (a), and the conditionally averaged PIV on plot (c). The selection event is a high frequency one, shown on plot (b). Plot (c) shows that the flow structures responsible for these high frequency events occur about a ¼ chord upstream of the probe in the gap: this is the region where the highest gap flow velocities are observed and subsequently the strongest gap perturbations are found. The cross-LIM analysis of pressure-pressure or of pressure-HWA measurements also allows reconstructing time signatures and phase speeds of selected events, which of course is not accessible with non time-resolved PIV.

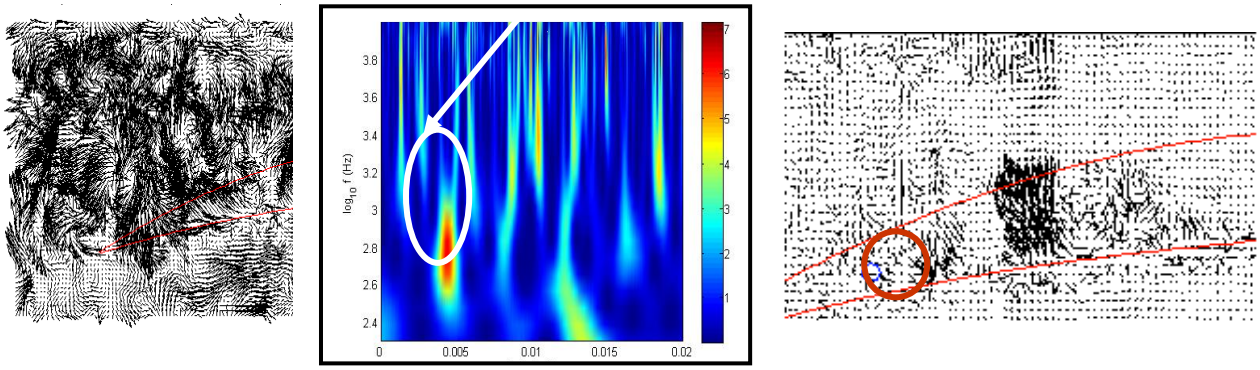

(a) Instantaneous velocity **(b) High frequency event (circle)** **(c) Conditional average**

Fig 4-5 Example of wavelet based conditional averaging ($U_0 = 70$ m/s; $h = 10$ mm, $\alpha = 15°$)

4.5 Space-time correlations

In aeroacoustics, space-time correlations are inputs for jet mixing noise models. In the present configurations space-time correlations might help modelling the source terms of the tip clearance jet that is evidenced in section 4.2 and 4.3. For practical reasons TR PIV could not be achieved in the upstream half chord region of the airfoil suction side. Here we illustrate the space-time correlation of the streamwise velocity fluctuation component on Fig 4-6: the correlation time in the $x = 2$ mm plane gives us an idea of the time a coherent structures takes to sweep past the TE. Subsequently the corresponding frequency may be estimated. In the example shown on Fig 4-6, the correlation time is about 2 to 5Δt, ($\Delta t = 0.33$ ms) thus the frequency is between 0.6 and 1.5 kHz, which is the frequency of the aforementioned hump in the wall pressure spectra: according to Fig 3-2, the streamwise velocity is about 1.4 times the inflow velocity, that is, 100 m/s: this leads to an eddy size ranging from 6 to 16 cm. The TLV diameter is about 5 cm and the vortical structures are likely to be stretched when they are accelerated around the vortex centre and convected downstream at high speed. This could explain the relatively large size derived from this analysis.

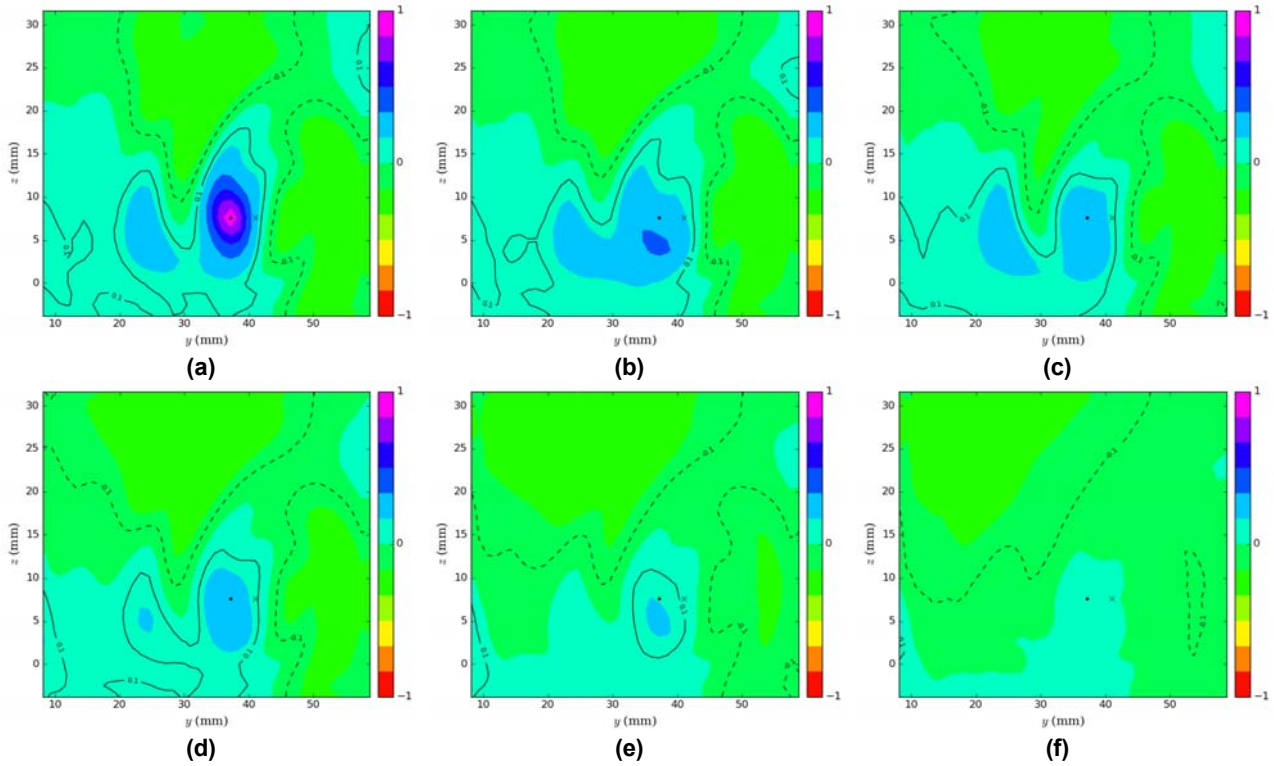

Fig 4-6 Two-point two-time correlation map for the streamwise velocity fluctuations for a point located 3.5 mm left of the vortex centre. From left to right and top to bottom, correlation time: $\tau = 0, \Delta t, 2\Delta t, 5\Delta t, 10\Delta t, 15\Delta t$. ($U_0 = 70$ m/s; $h = 10$ mm, $\alpha = 15°$)

5.0 SOUND RADIATED BY THE TIP CLEARANCE FLOW

5.1 Far field measurements

The far field measurements during phase 1 were carried out with a high background noise level. The far field spectra obtained at 1.5 m from the airfoil in the phase 1 experiments are plotted on plot (a) of Figure 5.1. As the noise levels with and without tip clearance are quite similar, the TE noise is estimated by computing the spectral difference between the two configurations. Since all the different types of sources are mutually uncorrelated broadband noise sources, the Power Spectral Density (PSD) level of the tip leakage noise $L_{PSD,tip}(f)$ can be obtained from the total PSD level $L_{PSD,tot}(f)$ and the PSD level measured without gap

$L_{PSD,no-gap}(f)$ by :

$$L_{PSD,tip}(f) = L_{PSD,tot}(f) + 10log_{10}\left(1 - 10^{-\left(L_{PSD,tot}(f) - L_{PSD,no-gap}(f)\right)}\right)$$

For measured far field differences that are relevant above 1dB, the tip noise spectrum can thus be obtained even if the tip noise is 5.8 dB below the background noise. The dominant tip noise frequency range is between 0.7 and $6-7$ kHz in both phases but in phase 1, the spectral difference was required to separate the tip clearance noise from the background noise. However the phase 1 chart shows that there are essentially two types of contributions.

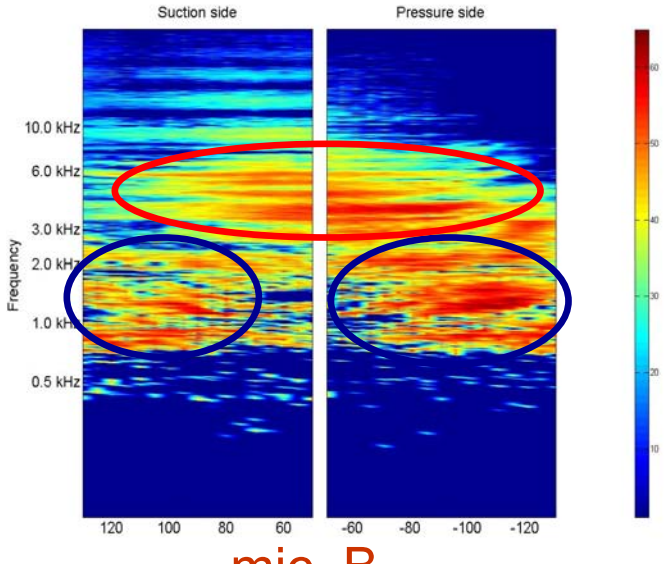

Phase 1 experiment

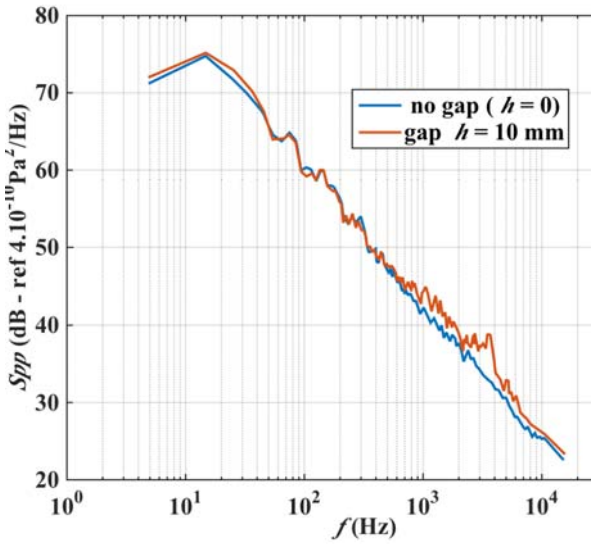

Phase 2 experiment (obs. angle 90° with respect the flow at 2m from airfoil)

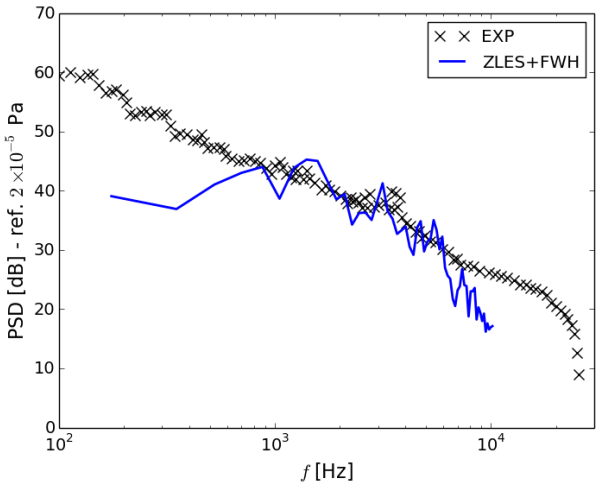

Comparison between the spectra obtained in phase 2 and by applying the FWH analogy to the ZLES data

Fig 5-1 far field obtained at each phase of the experiment: blue ellipses on left plot: medium frequency component; red ellipse on left plot: high frequency component. ($U_0 = 70$ m/s; $h = 10$ mm, $\alpha = 15°$)

The first is a medium frequency range (0.7 to 2.5 kHz) sound radiation that can be related to the hump

described in section 4. It is found to have a U^5 velocity dependence, which suggests a trailing edge type of source, that is, a source due to eddies convected at high speed past a geometrical singularity. In the present case it might as well be the airfoil trailing edge or the suction side airfoil tip edge.

Secondly, a high frequency component that might be related to the high frequency components of probe 19 is found. This is confirmed by the U^{7-8}velocity dependence of this high frequency component: it probably corresponds to the noise radiated by the tip leakage jet.

The two spectra plotted on the top right part of Fig 5-1 were obtained in phase 2, one with and the other without gap. The medium frequency hump due to the tip leakage flow appears very clearly on this plot. The frequencies agree with those highlighted on the top left plot, thus confirming the results and conclusions of the phase 1 measurements. The corresponding ZLES spectrum is shown on the bottom plot of Fig 5-1: it is in fair agreement with experimental one in the frequency range were the tip leakage noise is dominant.

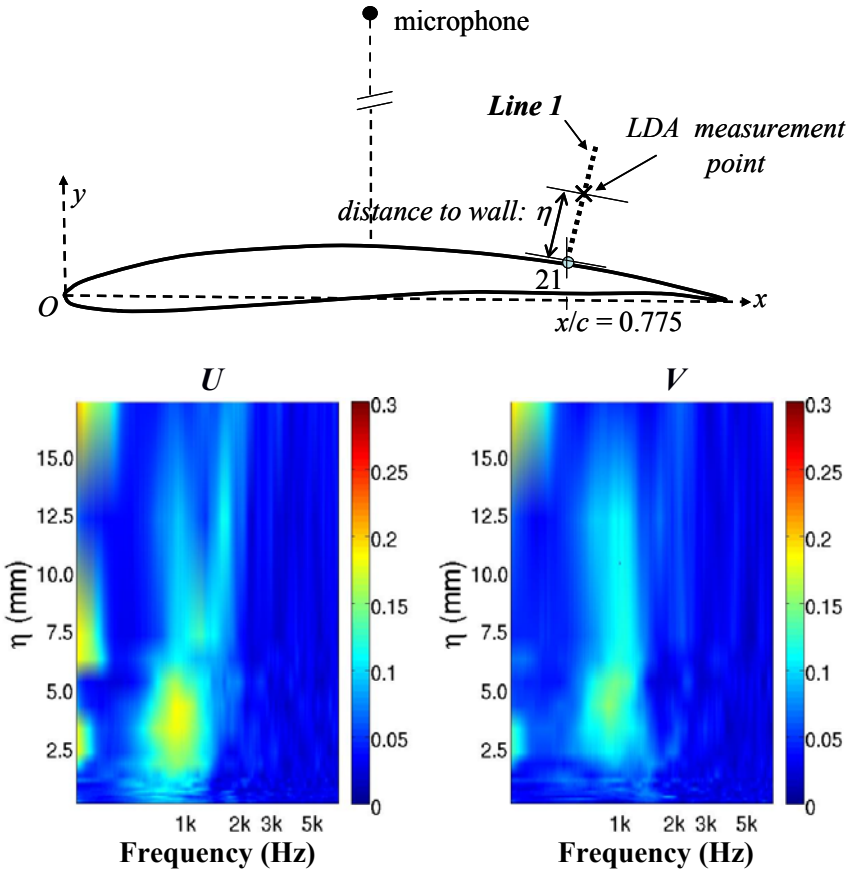

Fig 5.2 Near-to-far field coherence. The microphone is 1 m across the suction side at $x/c = 0.5$. Top plot: LDA measurement line (Line 1) for LDA-far field pressure coherence measurements. η is the distance from the current LDV measurement point to the wall at the position of probe 21 ($x = 0.775c = 155$ mm on the suction side). The microphone is 1 m across the suction side at $x/c = 0.5$. Velocity is non-dimensioned by the upstream velocity U_0. Velocity is made non-dimensional by the upstream velocity U_0. ($U_0 = 70$ m/s; $h = 10$ mm, $\alpha = 15°$)

5.2 Near-to-far field coherence

The LDV-pressure coherence analysis carried out in section 4.3 is repeated between the LDV probes and a far field located 1 m across the suction side. Results indicate that for frequencies comprised between 0.5 and 1.5 kHz typically, the far field is coherent with the velocity field in the vicinity of the wall ($\eta <$

6 *to* 7 mm) the maximal coherence being obtained at $\eta = 3 - 5$ mm and $f \sim 1$ kHz on the U component. It should be mentioned that although the values of the coherence remain quite low (less than 0.2), they are actually remarkably high, given the fact that each LDA measurement volume is indeed very small and that it is expected to contribute only weakly to the far field. This means that although the source is due to turbulence, it is quite concentrated in a narrow region near the airfoil tail. In other words, the sources of sound in the medium frequency range are due to coherent eddies passing nearby the trailing edge corner. This is consistent with the low frequency source 5^{th} power velocity dependence mentioned in the previous subsection. Similar conclusions haven been drawn in the previous section.

5.3 Far field wavelet analysis

The wavelet analysis carried out in the gap region (see section 4.4) is applied here between the PIV measurements in the gap region and the far field with a microphone located 1 m away from the airfoil, facing the suction side.

The conditionally averaged PIV field is shown on Fig 5.3. It confirms the presence of a large swirling flow region that is mainly concentrated in the gap near mid-chord, say between 40% and 60% chord typically which is linked to the far field. According to the detailed analysis of Camussi *et al.* [29], when examining the time delay observed between an event detected on the pressure probe at $3/4$ chord and the far field, this delay appears to be longer than the expected propagation time. This additional delay actually corresponds to the convection time between the probe position and the TE. Thus the sound is actually generated at the trailing edge as far as the medium frequency source is concerned although the radiating eddies are generated further upstream.

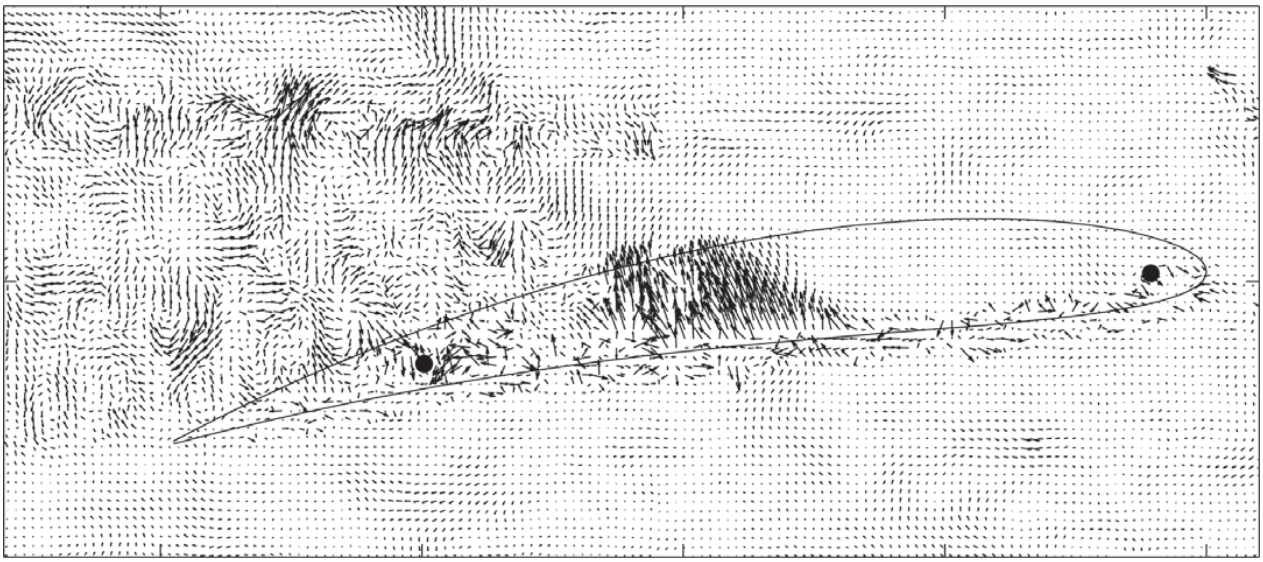

Fig 5.3 Conditional average of PIV measurement in the tip gap triggered by a far field microphone.

CONCLUSION

To conclude this application case, several aspects should be pointed out.

The first aspect is relative to the tip flow study itself. This investigation has highlighted the main self-noise source from a tip leakage flow as a trailing edge source due to eddies that are generated in the tip clearance and the TLV. Further the TLV has been studied in details and the small oscillations that have been found seem too weak to contribute significantly to the radiated noise. A different conclusion was drawn from a

TLV LES investigation that was carried out in a fan configuration: in that case, the neighbouring blades play probably an important role in the onset f these oscillations.

Moreover the study revealed a jet-like source and noise component but this was not further investigated due to the lack of measurements in the associated source region (upstream part of the airfoil). A dedicated experiment like a wall jet penetrating a cross-flow would help to characterise more precisely this source.

The two phases of the large experimental program described here, produced quite similar results as far as the TLV and more generally, the tip leakage flow were concerned. The main difference lies in the incoming boundary layer thickness: in phase 1, the boundary layer thickness was so large that the TLV noise was almost covered by boundary layer/leading edge interaction noise. During the phase 2 campaigns this noise component was suppressed or at least considerably reduced: subsequently, the tip leakage noise rose up to 5 dB above he background noise.

The second aspect is about the experimental techniques that have been applied. Although not all types of results have been shown in this lecture (*e.g.* no velocity spectrum has been included), a variety of techniques and post-processing approaches have contributed to the TLV study. Among these, one should distinguish the causality techniques (coherence, conditional wavelet analysis, space-time correlations) from the advanced running time measurements (TR PIV). Time Resolved PIV is indeed a measurement technique that progresses constantly and rapidly. It provides time evolution of complete flow regions and its time resolution will soon be fine enough to compute spectra that are relevant for aeroacoustic applications (see Lecture 1 § 4.1.1). The present application case illustrates perfectly well the variety of techniques and approaches one is likely to apply in order to extract relevant information about sound generation in complex flows.

The last aspect that should be mentioned is the benchmarking capacity of the tip leakage flow study. Although the present lecture is focused on the experimental approach, a few results were accompanied by ZLES results in order to illustrate the benchmarking aspect. Further details about CFD modelling of the present flow configuration can be found in literature cited hereafter.

REFERENCES

[1] J. Boudet, A. Cahuzac, P. Kausche, M.C. Jacob, Zonal large-eddy simulation of a fan tip-clearance flow with evidence of vortex wandering, *J. Turbo.*, **137**, 061001-9 pages, doi: 10.1115/1.4028668, (2015).

[2] A. McAlpine, M.J. Fisher, B.J. Tester, "Buzz-saw" noise: a comparison of measurement with prediction, *J. Sound and Vib*., **290**, 1202–1233, (2006).

[3] M.C. Jacob, J. Grilliat, R., Camussi, G., Caputi Gennaro, Aeroacoustic Investigation of a single airfoil tip leakage flow, *Int. J. Aeroacoustics*, **9(3)**, 253-272, (2010).

[4] M.C. Jacob, J. Jondeau, B. Li, Time resolved measurements of a tip leakage flow, *Int. J. Aeroacoustics*, **15 (6-7)**, 662-685, (2016).

[5] M.C. Jacob, J. Jondeau, B. Li, J. Boudet, Tip leakage flow: advanced measurements and analysis, *AIAA-paper n°* **2016-2823**, Lyon, France (2016).

[6] J. Boudet, G. Grilliat, J. Caro, M.C. Jacob, Combined experimental/computational study of tip clearance flow and acoustics, *8th European Turbomachinery Conference*, Graz, Austria, March, 23-27. (2009).

[7] J. Boudet, J. Caro, M.C. Jacob, Large-eddy simulation of a single airfoil tip clearance flow, *AIAA-paper n°* **2010-3978**, (2010).

[8] J. Boudet, B. Li, J. Caro, E. Jondeau, M.C. Jacob, Tip leakage flow: a detailed simulation with zonal approach, *AIAA paper n°* **2016-2824**, (2016).

[9] J. Boudet, J. Caro, B. Li, E. Jondeau, M.C. Jacob**,** Zonal large-eddy simulation of a tip-leakage flow, *Int. J. Aeroacoustics*, **15 (6-7)**, 646-661, (2016).

[10] J.P. Bindon, The measurement & formation of tip clearance loss, *J. Turbo.*, **111**, 257-263, (1989).

[11] M. Inoue, M. Kuroumaru, Structure of tip clearance flow in an isolated axial compressor rotor, *Trans. ASME*, **111**, 250-256, (1989).

[12] J.A. Storer, N.A. Cumpsty, Tip leakage flow in axial compressors, *Trans. ASME*, **113**, 252-259, (1991).

[13] B. Lakshlinarayana, M. Zaccaria, B. Marathe, The structure of tip clearance flow in axial flow compressors, *Trans. ASME*, **117**, 336-347, (1995).

[14] C. Muthanna, *Flowfield downstream of a compressor cascade with tip leakage*, Ms Thesis, Faculty of the Virginia Polytechnic Institute and State University, (1998).

[15] G. Tang, *Measurements of the tip-gap turbulent flow structure in a low-speed compressor cascade*, Ph.d. thesis, Faculty of the Virginia Polytechnic Institute and State University, (2004).

[16] N. Intaratep, *Formation and development of the tip leakage vortex in a simulated axial compressor with unsteady inflow*, Ph.d. thesis, Faculty of the Virginia Polytechnic Institute and State University, (2006).

[17] D. You, M. Wang, P. Moin, P. M. Mittal, Effects of tip-leakage flow in a turbomachinery cascade,

Phys. Fluids, **18(10)**, (2006).

[18] T. Fukano, Y. Takamatsu, The effects of tip clearance on the noise of low-pressure axial and mixed flow fans, *J. Sound Vib.*, **105**, 291-308 (1986).

[19] T. Fukano, C. Jang, Tip clearance noise of axial flow fans operating at design and off-design condition, *J. Sound Vib.*, **275**, 1027-1050 (2004).

[20] U.W. Ganz, T.J. Patten, D.F. Scharpf, P.D. Joppa, *Boeing 18-inch fan rig broadband noise test*. NASA CR-1998-208704, (1998).

[21] M.R. Khourrami, M. Choudari, A novel approach for reducing rotor tip-clearance induced noise in turbofan engines, *AIAA-paper n° 2001-2148***,** (2001).

[22] L. Neuhaus, W. Neise, Active flow control to improve the aerodynamic and acoustic performance of axial turbomachines, *AIAA paper n°* **2002- 2948***,* (2002).

[23] A. Corsini, B. Perugini, F. Rispoli, A.G. Sheard, I.R. Kinghorn, Experimental and numerical investigation on passive devices for tip clearance induced noise reduction in axial flow fans, *7th European Conference on Turbomachinery* (ECT-7), 5-9 March 2005, Athens, Greece

[24] A. Mann, M.-S. Kim, J. Wu, F. Perot, J. Grilliat, M.C. Jacob, M. Colman, Airfoil tip leakage aeroacoustics predictions using a lattice Boltzmann method, *AIAA Paper n°* **2016-2825**, (2016).

[25] M. Michard, L. Graftieaux, L., Lollini, N. Grosjean, Identification of Vortical Structures by a Non-Local Criterion: Application to PIV Measurements and DNS-LES Results of Turbulent Rotating Flows, *11th Symp. on turbulent shear flows,* Grenoble, France, (1997).

[26] L. Graftieaux, M. Michard, N. Grosjean, Combining PIV, POD, and Vortex Identification Algorithms for Study of Unsteady Turbulent Swirling Flows, *Meas. Sci. Tech*. **11**, 1422–1429, (2001).

[27] J. Grilliat, M.C. Jacob, R. Camussi, G. Caputi Gennaro, Experimental study of a tip leakage flow – part one: aerodynamic and acoustic measurements, *AIAA paper n°* **2007-3684**, (2007).

[28] R. Camussi and G. Guj, Orthonormal wavelet decomposition of turbulent flows: intermittency and coherent structures, *J. Fluid Mech*., **348**, 177-199, (1997).

[29] R. Camussi, J. Grilliat, G. Caputi-Gennaro, M.C. Jacob, Experimental study of a tip leakage flow: wavelet analysis of pressure fluctuations*, J. Fluid Mech*. **660**, 87-113, (2010).